

# Anchoring Sub-Nanometer Pt Clusters on Crumpled Paper-Like MXene Enables High Hydrogen Evolution Mass Activity

Yucai Wu, Wei Wei, Ruohan Yu, Lixue Xia, Xufeng Hong, Jiexin Zhu, Jiantao Li, Lei Lv, Wei Chen, Yan Zhao,\* Liang Zhou,\* and Liqiang Mai\*

Platinum (Pt)-based electrocatalysts are the benchmark catalysts for hydrogen evolution reaction (HER); however, they are limited by the scarcity and high price. Introducing an adequate substrate to disperse and anchor Pt-based species is a feasible pathway to improve the utilization efficiency. Herein, a quick and continuous spray drying route is proposed to fabricate 3D crumpled  $Ti_3C_2T_x$  MXene loaded with sub-nanometer platinum clusters (Pt/MXene). The 3D crumpled structure inhibits the restacking of layered MXene nanosheets and guarantees the fully exposure of Pt clusters. The as-prepared catalyst exhibits excellent HER performances comparable to commercial Pt/C, including a low overpotential of 34 mV to reach a current density of  $10 \text{ mA cm}^{-2}$ , a superior mass activity ( $1847 \text{ mA mg}_{Pt}^{-1}$ ), a small Tafel slope ( $29.7 \text{ mV dec}^{-1}$ ), and a high turnover frequency ( $10.66 \text{ H}_2 \text{ s}^{-1}$ ). The improved activity of Pt/MXene can be attributed to the charge transfer from Pt clusters to MXene, which weakens the hydrogen adsorption, as evidenced by the density functional theory calculations. The present contribution proposes a novel strategy to anchor low-mass-loading sub-nanometer precious metal clusters on crumpled MXene with fully exposed active sites for catalysis.

hydrogen energy has become one of the most promising technologies due to its high heating value and environmental friendliness.<sup>[1]</sup> Hydrogen evolution reaction (HER) is a part section of electrochemistry water splitting. Compared to the oxygen evolution reaction, the HER has faster kinetics as well as lower overpotential.<sup>[2]</sup> Noble metals like platinum (Pt) have been proved as benchmarking catalysts for HER.<sup>[3]</sup> However, the high price and rareness of Pt resources hamper the widespread application. Reducing the dosage and size of Pt in catalysts are promising strategies to tackle this bottleneck. However, with the reduce of size to sub-nanometer scale, the Pt particles tend to aggregate, leading to deteriorated activity. Placing Pt species on appropriate substrates would be a promising tactic to stabilize Pt sub-nanometer clusters.<sup>[4]</sup>

MXenes, first reported in 2011, are a new type of 2D transition metal carbides

and nitrides. Benefited from its unique physiochemical features, such as high conductivity, affluent surface termination groups, outstanding hydrophilicity, and synthetic diversity, MXene has attracted great attention in secondary batteries,<sup>[5]</sup> supercapacitors,<sup>[6]</sup> electromagnetic shielding,<sup>[7]</sup> sensors,<sup>[8]</sup> and photo/electrocatalysts.<sup>[9]</sup> In addition, defects can be formed on the surface during the etching process of MAX, and they can serve as anchoring sites to confine noble atoms/clusters.<sup>[10]</sup> The high specific surface area of MXene guarantees the high dispersion of noble metal catalysts. The high conductivity and surface termination groups may bring strong interactions between the MXene and noble metals, effectively modulating the catalytic activity. Thus, MXene would be a model carrier to support precious metal catalysts like Pt. Nevertheless, MXene nanosheets are inclined to self-stacking because of the relatively high surface energy and strong interlayer van der Waals force, which prevents the exposure of catalytic active sites. Conventional drying processes could not avoid the agglomeration. Novel drying techniques, such as spray-drying and freeze-drying are able to remit the self-stacking of MXene nanosheets. Especially, the spray drying is a quick and continuous technique to transform the 2D nanosheets into 3D crumpled paper-like structures, which could minimize the aggregation and maximize the exposure of active sites.

## 1. Introduction

With the rapid development of society, the energy issue has received increasing attention. Owing to the unsustainability of fossil fuels and limitations of wind, tide, and solar energy,

Y. Wu, W. Wei, R. Yu, X. Hong, J. Zhu, J. Li, L. Lv, W. Chen, L. Zhou, L. Mai  
State Key Laboratory of Advanced Technology for Materials Synthesis  
and Processing

Wuhan University of Technology  
Wuhan 430070, P. R. China

E-mail: liangzhou@whut.edu.cn; mlq518@whut.edu.cn

L. Xia, Y. Zhao

International School of Materials Science and Engineering

Wuhan University of Technology  
Wuhan 430070, P. R. China

E-mail: yan2000@whut.edu.cn

W. Chen

Hubei Key Laboratory of Ferro and Piezoelectric Materials and Devices

Hubei University

Wuhan 430062, P. R. China

 The ORCID identification number(s) for the author(s) of this article  
can be found under <https://doi.org/10.1002/adfm.202110910>.

DOI: 10.1002/adfm.202110910

Herein, we report a quick and continuous spray drying route to construct 3D crumpled paper-like MXene with sub-nanometer Pt cluster decorations. The Pt species were spontaneously reduced and immobilized on the MXene nanosheets, and the 3D crumpled structure not only minimizes the self-stacking/agglomeration of 2D MXene nanosheets but also maximizes the exposure of Pt catalysts. The Pt/MXene demonstrates efficient HER performance, including a diminutive overpotential of 34 mV at the conventional current density of  $10 \text{ mA cm}^{-2}$  and distinguished mass activity of  $1847 \text{ mA mg}_{\text{Pt}}^{-1}$ . Such performances surpass the commercial Pt/C catalyst ( $265 \text{ mA mg}_{\text{Pt}}^{-1}$  at the overpotential of 50 mV). Theoretical calculations uncover that the interaction between Pt cluster and MXene ensures appropriate Gibbs hydrogen adsorption free energy ( $\Delta G_{\text{H}^*}$ ), which is beneficial for the HER activity.

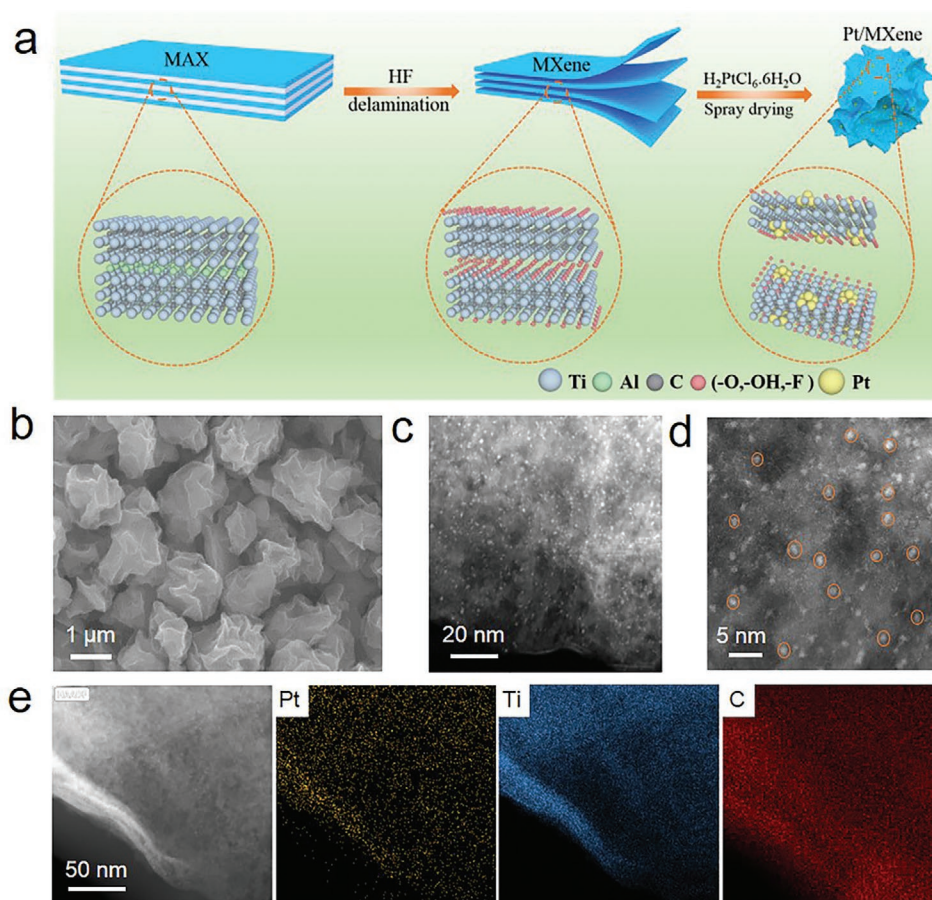
## 2. Results and Discussion

The preparation route of Pt/MXene electrocatalyst is schematically shown in Figure 1a. In short, accordion-like  $\text{Ti}_3\text{C}_2\text{T}_x$  MXene was fabricated by HF etching of the  $\text{Ti}_3\text{AlC}_2$  precursor, which removes the Al layer.<sup>[11]</sup> After tetramethylammonium hydroxide intercalation and ultrasonic delamination, few-layer

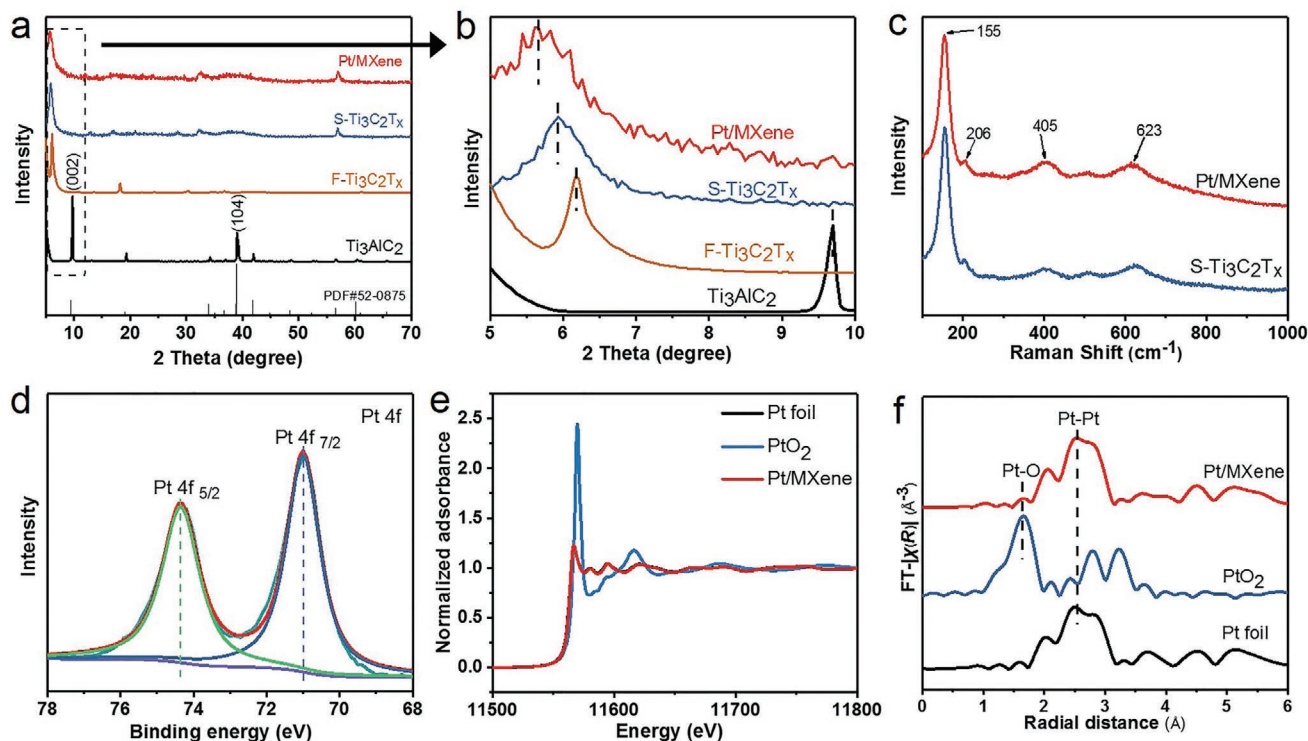
$\text{Ti}_3\text{C}_2\text{T}_x$  nanosheets can be obtained. To synthesize Pt/MXene catalysts, the  $\text{Ti}_3\text{C}_2\text{T}_x$  colloid suspension was mixed with dilute  $\text{H}_2\text{PtCl}_6 \cdot 6\text{H}_2\text{O}$  solution and spray dried.<sup>[12]</sup> Owing to the existence of low-valence-state Ti (II and III) in the  $\text{Ti}_3\text{C}_2\text{T}_x$  MXene, the Pt (IV) species were spontaneously reduced to single atom Pt and sub-nanometer Pt clusters and immobilized near the defects.<sup>[13]</sup>

Figure S1 of the Supporting Information presents the scanning electron microscopy (SEM) images of the MAX, accordion-like  $\text{Ti}_3\text{C}_2\text{T}_x$  MXene, freeze-dried  $\text{Ti}_3\text{C}_2\text{T}_x$  MXene, and spray-dried  $\text{Ti}_3\text{C}_2\text{T}_x$  MXene. Interestingly, the samples obtained by freeze-drying and spray-drying exhibit completely different morphologies (Figure S1c,d, Supporting Information). The freeze-dried sample (denoted as F- $\text{Ti}_3\text{C}_2\text{T}_x$ ) exhibits an agglomerated morphology. By contrast, the spray-dried sample (denoted as S- $\text{Ti}_3\text{C}_2\text{T}_x$ ) exhibits a 3D corrugated paper-like morphology, which can be ascribed to assembly and collapse of 2D  $\text{Ti}_3\text{C}_2\text{T}_x$  nanosheets caused by the evaporation of solvent during the spray-drying process.

SEM image shows the 3D crumpled structure of Pt/MXene (Figure 1b), suggesting that the introduction of  $\text{H}_2\text{PtCl}_6$  in precursor solution does not alter the morphology of the product. Transmission electron microscopy (TEM) picture in-depth affirms the 3D crumpled structure (Figure S2, Supporting



**Figure 1.** a) Schematic illustration for the preparation of Pt/MXene. b) SEM images of Pt/MXene. c,d) HAADF-STEM images of Pt/MXene and e) the EDX elemental mappings.



**Figure 2.** a) XRD patterns of the Ti<sub>3</sub>AlC<sub>2</sub>, F-Ti<sub>3</sub>C<sub>2</sub>T<sub>x</sub>, S-Ti<sub>3</sub>C<sub>2</sub>T<sub>x</sub>, and Pt/MXene. b) Magnified XRD patterns showing the 2θ region from 5° to 10°. c) Raman spectra of Pt/MXene and S-Ti<sub>3</sub>C<sub>2</sub>T<sub>x</sub>. d) Pt 4f XPS spectrum of the Pt/MXene. e) Normalized Pt L<sub>3</sub>-edge XANES and f) FT k<sub>3</sub>χ(R) Pt L<sub>3</sub>-edge EXAFS spectra for Pt/MXene, Pt foil, and PtO<sub>2</sub>.

Information). High-angle annular dark-field scanning transmission electron microscopy (HAADF-STEM) and energy dispersive X-ray (EDX) elemental mapping were used for further studying the distribution of Pt on Ti<sub>3</sub>C<sub>2</sub>T<sub>x</sub> MXene. As displayed in Figure 1c,d, the sub-nanometer Pt clusters with uniform size evenly anchored on the surface of MXene. Inevitably, some single-atomic Pt also present on the surface. The EDX mappings also confirm that the Pt clusters and single atoms disperse homogeneously on MXene (Figure 1e). As is well-known, Ti defects could be formed on the surface of MXene during the HF etching, and can serve as sites to anchor metal atoms. Thus, we speculate that the Pt atoms are trapped by Ti defects. Through inductively coupled plasma-optical emission spectroscopy test, the Pt loading amount is determined to be ≈2.9 wt%.

The as-prepared Ti<sub>3</sub>C<sub>2</sub>T<sub>x</sub> MXene suspension exhibits obvious colloidal property and there is no obvious sediments in the suspension after 42 days as shown in the optical photographs (Figure S3a, Supporting Information).<sup>[14]</sup> The good stability in solution may profit from the strong electrostatic repulsions between few-layer MXene. However, the multilayer MXene often leads to sediments and restacking behavior. Zeta potential is chosen to further study the stability of the as-prepared Ti<sub>3</sub>C<sub>2</sub>T<sub>x</sub> MXene colloidal suspension. The Zeta potential of the initial Ti<sub>3</sub>C<sub>2</sub>T<sub>x</sub> MXene colloidal solution is -21.4 mV, whereas the solution standing for 42 days shows a Zeta potential of -19.6 mV (Figure S3b, Supporting Information), certifying the favorable stability. The surface charge density of MXene decreases after drying, either freeze-drying or spray-drying, which may be caused by the alteration of termination groups during drying

(Figure S3c, Supporting Information). The surface charge density further decreases after Pt loading, which may be caused by the charge transfer between MXene and the Pt.

The F-Ti<sub>3</sub>C<sub>2</sub>T<sub>x</sub> nanoflakes manifest a specific surface area of 1.9 m<sup>2</sup> g<sup>-1</sup> as determined by Brunauer-Emmett-Teller (BET) N<sub>2</sub> sorption (Figure S4, Supporting Information).<sup>[15]</sup> On the contrary, the 3D crumpled S-Ti<sub>3</sub>C<sub>2</sub>T<sub>x</sub> MXene exhibits a larger BET surface area of 7.2 m<sup>2</sup> g<sup>-1</sup>, which is almost quadruple that of F-Ti<sub>3</sub>C<sub>2</sub>T<sub>x</sub>. The increase in specific surface area suggests that the assembly of 2D MXene nanosheets to 3D crumpled structure can effectively avoid their restacking. The obtained various specimens are further characterized with the aid of X-ray diffraction (XRD). The (104) diffraction peak of Ti<sub>3</sub>AlC<sub>2</sub> disappears after HF etching, suggesting the successful removal of Al layers (Figure 2a).<sup>[16]</sup> Meanwhile, the (002) peak of Ti<sub>3</sub>AlC<sub>2</sub> MAX phase at 9.7° shifts to a lower angle of 6.2° for F-Ti<sub>3</sub>C<sub>2</sub>T<sub>x</sub> (Figure 2b). Compared to the F-Ti<sub>3</sub>C<sub>2</sub>T<sub>x</sub>, the (002) diffraction of S-Ti<sub>3</sub>C<sub>2</sub>T<sub>x</sub> presents a further shift toward lower angles (6.2° for F-Ti<sub>3</sub>C<sub>2</sub>T<sub>x</sub>, 5.9° for S-Ti<sub>3</sub>C<sub>2</sub>T<sub>x</sub>) and broadening, indicating the increased interplanar spacing and decreased layer thickness of S-Ti<sub>3</sub>C<sub>2</sub>T<sub>x</sub> MXene.<sup>[17]</sup> No characteristic diffractions for Pt can be observed in the XRD pattern of Pt/MXene, which can be ascribed to the ultrafine size and relatively low loading amount of Pt (≈2.9 wt%). Raman spectroscopy (Figure 2c) provides further structural information on S-Ti<sub>3</sub>C<sub>2</sub>T<sub>x</sub> and Pt/MXene. Specifically, the peak at 155 cm<sup>-1</sup> of Pt/MXene corresponds to the A<sub>1g</sub> symmetry out-of-plane vibrations of the Ti<sub>3</sub>C<sub>2</sub>T<sub>x</sub>. The strong peak at about 206 cm<sup>-1</sup> can be attributed to the A<sub>1g</sub> mode of Ti<sub>3</sub>C<sub>2</sub>O<sub>2</sub>,<sup>[18]</sup> while the band at 623 cm<sup>-1</sup> corresponds to the E<sub>g</sub> mode of Ti<sub>3</sub>C<sub>2</sub>F<sub>2</sub>.<sup>[19]</sup>

Besides, the representative Raman band at  $405\text{ cm}^{-1}$  of  $\text{Ti}_3\text{C}_2\text{T}_x$  is also observed.

In order to dissect the chemical states and surface groups on the samples, X-ray photoelectron spectroscopy (XPS) was adopted. A certain amount of F termination groups exist in the sample as evidenced from the XPS survey spectrum of S- $\text{Ti}_3\text{C}_2\text{T}_x$  MXene (Figure S5) and Table S1, Supporting Information). As for the high-resolution Pt 4f spectra of Pt/MXene, the peaks at 71.0 and 74.3 eV are referred to  $\text{Pt}^0 4f_{7/2}$  and  $\text{Pt}^0 4f_{5/2}$ , respectively (Figure 2d).<sup>[20]</sup> From the Al 2p spectra (Figures S6a and S7a, Supporting Information), we can know that the etching process fully removes the Al layer from the MAX precursor.<sup>[21]</sup> The Ti 2p spectrum of  $\text{Ti}_3\text{AlC}_2$  MAX can be divided into three bonding types, that is Ti–Al, Ti–C, and Ti–O (Figure S6b and Table S2, Supporting Information). As for the Pt/MXene, the Ti 2p spectrum shows four  $2p_{1/2}$ – $2p_{3/2}$  doublets, corresponding to Ti–C, C–Ti<sup>2+</sup>–(O/OH), C–Ti<sup>3+</sup>–(O/OH), and  $\text{TiO}_{2-x}\text{F}_{2x}$ . (Figure S7b and Table S3, Supporting Information).<sup>[22]</sup> Among these Ti species, the C–Ti<sup>3+</sup>–(O/OH) shows the largest portion, which is caused by the surface oxidation of MXene nanosheets. Given the existence of Ti<sup>2+</sup> in the  $\text{Ti}_3\text{C}_2\text{T}_x$  MXene, it is deduced that the  $[\text{PtCl}_6]^{2-}$  ions were reduced to Pt by such highly reductive Ti species. For the C 1s signal of Pt/MXene, components at 283.1, 284.5, and 287.1 eV appointed as C–Ti/Pt, C–C, and C–O bonds, respectively (Figure S7c, Supporting Information).<sup>[23]</sup> For the O 1s of Pt/MXene, the Ti–O,  $\text{TiO}_{2-x}\text{F}_{2x}$ , C–Ti–O, and C–Ti–OH are located at 528.1, 528.9, 530.3, and 531.1 eV, respectively (Figure S7d, Supporting Information).<sup>[24]</sup>

To get further insight into the electronic states and coordination environment of the Pt species on MXene, X-ray absorption spectroscopy was performed. Figure 2e exhibits the normalized

Pt L<sub>3</sub>-edge X-ray absorption near-edge structure (XANES) curves of Pt foil,  $\text{PtO}_2$ , and Pt/MXene. The intensity of optimized Pt/MXene is apparently lower than that of  $\text{PtO}_2$ , but overlaps with that of Pt foil, demonstrating that the Pt species on MXene exist in the form of  $\text{Pt}^0$  (consistent with the XPS result). The magnified pre-edge profiles further confirm this conclusion (Figure S8, Supporting Information). The Fourier-transform extended X-ray absorption fine structure spectroscopy (EXAFS) of Pt/MXene shows a distinct Pt–Pt peak (Figure 2f). A minor Pt–O peak can also be observed at 1.62 Å, suggesting the Pt clusters might be stabilized by Ti–O surface termination groups on MXene.

The HER performance of Pt/MXene was carried out through a representative three-electrode equipment in 0.5 M  $\text{H}_2\text{SO}_4$  electrolyte with a virgin graphite rod as the counter electrode. Figure 3a indicates the HER polarization plots of S- $\text{Ti}_3\text{C}_2\text{T}_x$  MXene, Pt/C, and Pt/MXene. The S- $\text{Ti}_3\text{C}_2\text{T}_x$  MXene shows poor HER performance, and it demands an overpotential of 247 mV at the same current density of  $\eta_{10}$ . With the loading of Pt, the Pt/MXene demonstrates nearly zero onset potential ( $\eta_{\text{onset}}$ ) and the lowest overpotential of 34 mV to reach the specific current density ( $\eta_{10}$ ). The above results are comparable to the state-of-the-art commercial Pt/C electrocatalyst (37 mV). Furthermore, at a higher current density of  $100\text{ mA cm}^{-2}$ , the expectant Pt/MXene also exhibits a low overpotential of 185 mV (Figure 3b). The current densities of Pt/MXene and Pt/C are normalized to the loading of Pt to investigate the mass activity of catalysts, which can more objectively reflect the catalytic activity. As shown in Figure 3c the Pt/MXene exhibits much better HER performance in mass activity compared with the business-like 20 wt% Pt/C. Specifically, the Pt/MXene demonstrates a mass activity of  $1847\text{ mA mg}_{\text{Pt}}^{-1}$  at the overpotential of 50 mV, which is seven

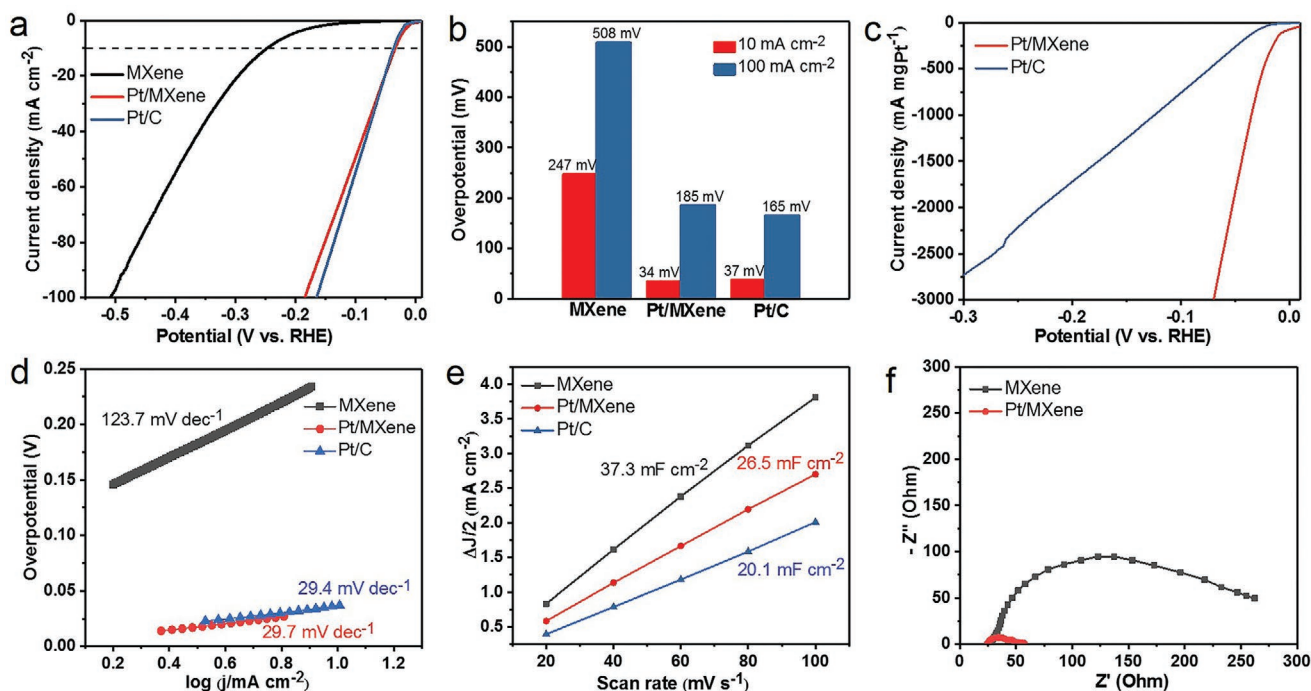


**Figure 3.** a) Polarization curves of MXene, Pt/MXene, and Pt/C. b) Specific activity of MXene, Pt/MXene, and Pt/C at  $j_{10}$  and  $j_{100}$ . c) Mass activity of Pt/MXene and Pt/C. d) Tafel slope derived from (a). e) Double-layer capacitance ( $C_{dl}$ ) plots of MXene, Pt/MXene, and Pt/C. f) EIS spectra of MXene and Pt/MXene.

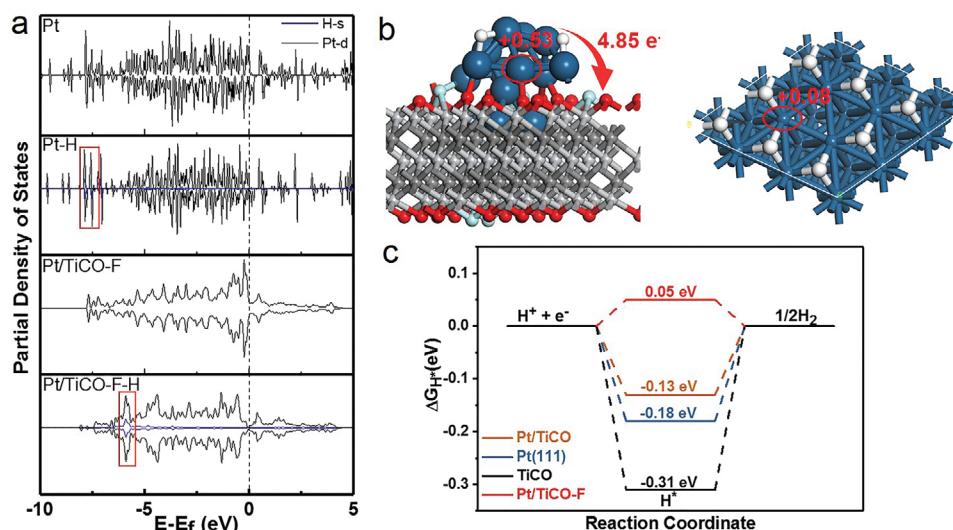


**Figure 4.** a) PDOS of Pt and Pt/TiCO-F. b) Bader charge distribution of Pt/TiCO-F and Pt. Atoms in blue, white, red, cyan, gray, and dark gray represent Pt, H, O, F, Ti, and C, respectively. c) The calculated free energy diagram for hydrogen evolution on Pt/TiCO, Pt(111), TiCO, and Pt/TiCO-F. Annotation: TiCO refers to the MXene with oxygen termination groups. TiCO-F refers to the MXene with oxygen and fluorine termination groups.

times to than that of Pt/C. The results indicate that the Pt clusters anchored on 3D crumpled MXene are capable of delivering higher HER mass activity than industrialized Pt/C catalyst, and the 3D crumpled structure of MXene with maximized exposure of Pt are responsible for the superior mass activity.

To explore the reaction kinetics of the as-prepared catalysts, we calculate the Tafel slope to analyze the rate-determining step during the HER process. Generally, the HER in acid solution can be broadly divided into two steps. The first one is that protons received electrons to form intermediates (Volmer reaction:  $\text{H}^+ + \text{e}^- \rightarrow \text{H}^*$ ), and the next step is the different desorption path of intermediates hydrogen (Heyrovsky reaction:  $\text{H}^* + \text{H}^+ + \text{e}^- \rightarrow \text{H}_2$  or Tafel reaction:  $\text{H}^* + \text{H}^* \rightarrow \text{H}_2$ ).<sup>[25]</sup> The Tafel slopes of Pt/MXene and Pt/C are 29.7 and 29.4 mV dec<sup>-1</sup> (Figure 3d), respectively. From the Tafel slope value manifests that the Pt/MXene electrocatalyst follows the Volmer–Tafel mechanism with a fast primary discharge step but restricted to a slow recombination step.

The electrochemically active surface area (ECSA) test was performed to calculate the double-layer capacitance ( $C_{dl}$ ) (Figure S9, Supporting Information).<sup>[26]</sup> The Pt/MXene possesses a significantly higher  $C_{dl}$  (26.5 mF cm<sup>-2</sup>) than Pt/C (20.1 mF cm<sup>-2</sup>), indicating the larger ECSA of Pt/MXene (Figure 3e). The enlarged ECSA of Pt/MXene illustrates that more active sites are exposed and thus enhances the HER performance, which is benefited from the 3D crumpled paper-like structure of MXene. The turnover frequency (TOF) is a significant indicator to estimate the intrinsic activity of electrocatalysts. The Pt/MXene exhibits high TOF values of 10.66 H<sub>2</sub> s<sup>-1</sup> at the overpotential of 200 mV, which is remarkably higher than that of the state-of-the-art Pt/C electrocatalyst (Figure S10, Supporting Information). Electrochemical impedance spectroscopy (EIS) is adopted to further scrutinize the HER kinetics behavior.<sup>[27]</sup> The Pt/MXene reveals a smaller charge transfer resistance than the S-Ti<sub>3</sub>C<sub>2</sub>T<sub>x</sub> MXene (Figure 3f), which may be associated with the high conductivity of MXene substrate and the electron interac-

tion between Pt clusters and MXene. The stability is an important factor for HER catalyst. Over 10 000 s continuous chronopotentiometry measurement, the Pt/MXene shows a small potential drop of only 9 mV (Figure S11, Supporting Information). In addition, the microstructure of Pt/MXene maintains well after the durability test (Figure S12, Supporting Information). On the contrary, the performance of commercial Pt/C decreases obviously after 6000 s. Compared with earlier reports on Pt-based or MXene-based HER catalysts, the constructed Pt/MXene composites show obviously lower overpotential toward HER in acidic solution (Figure S13, Supporting Information).

We further carried out density functional theory (DFT) computations to get more insight into the interaction between Pt clusters and MXene (TiCO and TiCO-F). The models of Pt/TiCO-F-H, Pt/TiCO-H, Pt(111)-H, and TiCO-H are constructed for DFT simulation (Figure S14, Supporting Information). The partial density of state (PDOS) shows that the d-band center of Pt in Pt/MXene (Pt/TiCO-F) is closer to the Fermi level than that of Pt (Figure 4a), suggesting the antibonding orbital offers more contribution and results in an adsorption capacity that is neither too strong nor too weak.<sup>[28]</sup> The red rectangular areas represent the combination of Pt and H. With positive shift for Pt/TiCO-F, the binding capacity of Pt to H is weakened. The Bader charge distribution clearly shows that the electrons transfer from Pt clusters to the TiCO-F matrix, resulting in +0.53 positive charge per Pt site, and thus impairs the Pt–H bonding (Figure 4b). As shown in Figure 4c, the Gibbs free energy for hydrogen adsorption ( $\Delta G_{\text{H}^*}$ ) of TiCO is calculated to be -0.31 eV, indicating the strong hydrogen adsorption on TiCO. Due to weakened hydrogen adsorption, the calculated  $\Delta G_{\text{H}^*}$  for Pt/TiCO-F is only 0.05 eV, which is lower than Pt(111) (-0.18 eV) and Pt/TiCO (-0.13 eV). From the above discussions, it is concluded that the introduction of oxygen and fluorine termination groups on MXene can effectively enhance the interaction with Pt clusters and thus the electronic states. The weakened hydrogen adsorption leads to easier hydrogen desorption and insures the superior HER catalytic activity of Pt/MXene.

### 3. Conclusion

In summary, an efficient Pt/MXene HER electrocatalyst featuring sub-nanometer Pt clusters anchored on 3D crumpled paper-like MXene has been constructed. With a low platinum loading amount of 2.9 wt%, the obtained Pt/MXene catalyst demonstrates an HER performance comparable with mercantile Pt/C catalyst with an exorbitant platinum loading amount of 20 wt% in terms of overpotential and Tafel slope. Moreover, the Pt/MXene demonstrates a mass activity of 1847 mA mg<sub>Pt</sub><sup>-1</sup> at the overpotential of 50 mV, seven times to that of commercial Pt/C. Meanwhile, DFT computations reveal the electron transfer from Pt to MXene with the termination groups of oxygen and fluorine, which weakens the hydrogen adsorption on Pt and facilitates its desorption. This study provides insight on the rational design of low-Pt catalysts for HER.

### Supporting Information

Supporting Information is available from the Wiley Online Library or from the author.

### Acknowledgements

Y.W., W.W., and R.Y. contributed equally to this work. This work was supported by the National Key Research and Development Program of China (2020YFA0715004), National Natural Science Foundation of China (51832004), Foshan Xianhu Laboratory of the Advanced Energy Science and Technology Guangdong Laboratory (XHT2020-003), Open Project Fund of Hubei Provincial Key Laboratory of Ferroelectric Materials and Devices (K202003), the Fundamental Research Funds for the Central Universities (2020III 004GX and 202010497004). The authors thank the Beamline 12-BM-B at the Advanced Photon Source for XAFS measurements. This S/TEM work was performed at the Nanostructure Research Center (NRC), which was supported by the State Key Laboratory of Advanced Technology for Materials Synthesis and Processing, and the State Key Laboratory of Silicate Materials for Architectures (all the laboratories are at Wuhan University of Technology).

### Conflict of Interest

The authors declare no conflict of interest.

### Data Availability Statement

The data that support the findings of this study are available from the corresponding author upon reasonable request.

### Keywords

crumpled MXene, hydrogen evolution reaction, spray-drying, sub-nanometer Pt cluster

Received: October 27, 2021  
Revised: December 16, 2021  
Published online:

- [1] Z. W. Seh, J. Kibsgaard, C. F. Dickens, I. Chorkendorff, J. K. Nørskov, T. F. Jaramillo, *Science* **2017**, *355*, 4998.
- [2] L. Bai, X. Wen, J. Guan, *Mater. Today Energy* **2019**, *12*, 311.
- [3] C. Li, Z. Chen, H. Yi, Y. Cao, L. Du, Y. Hu, F. Kong, R. Kramer Campen, Y. Gao, C. Du, G. Yin, I. Y. Zhang, Y. Tong, *Angew. Chem., Int. Ed.* **2020**, *59*, 15902.
- [4] Z. Ma, H. Tian, G. Meng, L. Peng, Y. Chen, C. Chen, Z. Chang, X. Cui, L. Wang, W. Jiang, J. Shi, *Sci. China Mater.* **2020**, *63*, 2517.
- [5] C. Sun, X. Shi, Y. Zhang, J. Liang, J. Qu, C. Lai, *ACS Nano* **2020**, *14*, 1176.
- [6] C. Couly, M. Alhabeab, K. L. Van Aken, N. Kurra, L. Gomes, A. M. Navarro-Suárez, B. Anasori, H. N. Alshareef, Y. Gogotsi, *Adv. Electron. Mater.* **2018**, *4*, 1700339.
- [7] T. Yun, H. Kim, A. Iqbal, Y. S. Cho, G. S. Lee, M. K. Kim, S. J. Kim, D. Kim, Y. Gogotsi, S. O. Kim, C. M. Koo, *Adv. Mater.* **2020**, *32*, 1906769.
- [8] S. J. Kim, H. J. Koh, C. E. Ren, O. Kwon, K. Maleski, S. Y. Cho, B. Anasori, C. K. Kim, Y. K. Choi, J. Kim, Y. Gogotsi, H. T. Jung, *ACS Nano* **2018**, *12*, 986.
- [9] S. Cao, B. Shen, T. Tong, J. Fu, J. Yu, *Adv. Funct. Mater.* **2018**, *28*, 1800136.
- [10] a) X. Sang, Y. Xie, M. W. Lin, M. Alhabeab, K. L. Van Aken, Y. Gogotsi, P. R. C. Kent, K. Xiao, R. R. Unocic, *ACS Nano* **2016**, *10*, 9193; b) D. Zhao, Z. Chen, W. Yang, S. Liu, X. Zhang, Y. Yu, W. C. Cheong, L. Zheng, F. Ren, G. Ying, X. Cao, D. Wang, Q. Peng, G. Wang, C. Chen, *J. Am. Chem. Soc.* **2019**, *141*, 4086.
- [11] M. Naguib, M. Kurtoglu, V. Presser, J. Lu, J. Niu, M. Heon, L. Hultman, Y. Gogotsi, M. W. Barsoum, *Adv. Mater.* **2011**, *23*, 4248.
- [12] X. Li, M. Zhang, W. You, K. Pei, Q. Zeng, Q. Han, Y. Li, H. Cao, X. Liu, R. Che, *ACS Appl. Mater. Interfaces* **2020**, *12*, 18138.
- [13] Z. Zhang, H. Li, G. Zou, C. Fernandez, B. Liu, Q. Zhang, J. Hu, Q. Peng, *ACS Sustainable Chem. Eng.* **2016**, *4*, 6763.
- [14] G. Ying, A. D. Dillon, A. T. Fafarman, M. W. Barsoum, *Mater. Res. Lett.* **2017**, *5*, 391.
- [15] a) W. Bao, X. Tang, X. Guo, S. Choi, C. Wang, Y. Gogotsi, G. Wang, *Joule* **2018**, *2*, 778; b) Q. X. Xia, J. Fu, J. M. Yun, R. S. Mane, K. H. Kim, *RSC Adv.* **2017**, *7*, 11000.
- [16] Z. Cao, Y. Yang, Y. Zheng, W. Wu, F. Xu, R. Wang, J. Sun, *J. Mater. Chem. A* **2019**, *7*, 25314.
- [17] X. Zhao, A. Vashisth, E. Prehn, W. Sun, S. A. Shah, T. Habib, Y. Chen, Z. Tan, J. L. Lutkenhaus, M. Radovic, M. J. Green, *Matter* **2019**, *1*, 513.
- [18] X. Feng, J. Ning, B. Wang, H. Guo, M. Xia, D. Wang, J. Zhang, Z.-S. Wu, Y. Hao, *Nano Energy* **2020**, *72*, 104741.
- [19] T. Zhou, C. Wu, Y. Wang, A. P. Tomsia, M. Li, E. Saiz, S. Fang, R. H. Baughman, L. Jiang, Q. Cheng, *Nat. Commun.* **2020**, *11*, 2077.
- [20] a) K. Jiang, B. Liu, M. Luo, S. Ning, M. Peng, Y. Zhao, Y. R. Lu, T. S. Chan, F. M. F. de Groot, Y. Tan, *Nat. Commun.* **2019**, *10*, 1743; b) M. Tavakkoli, N. Holmberg, R. Kronberg, H. Jiang, J. Sainio, E. I. Kauppinen, T. Kallio, K. Laasonen, *ACS Catal.* **2017**, *7*, 3121.
- [21] a) G. Mu, D. Mu, B. Wu, C. Ma, J. Bi, L. Zhang, H. Yang, F. Wu, *Small* **2020**, *16*, 1905430; b) S. Myhra, J. A. A. Crossley, M. W. Barsoum, *J. Phys. Chem. Solids* **2001**, *62*, 811.
- [22] a) Y. Fang, R. Lian, H. Li, Y. Zhang, Z. Gong, K. Zhu, K. Ye, J. Yan, G. Wang, Y. Gao, Y. Wei, D. Cao, *ACS Nano* **2020**, *14*, 8744; b) J. Li, K. Han, J. Huang, G. Li, S. Peng, N. Li, J. Wang, W. Zhang, Y. Du, Y. Fan, W. Wang, F. Dang, *Energy Storage Mater.* **2021**, *35*, 669.
- [23] J. Tang, T. S. Mathis, N. Kurra, A. Sarycheva, X. Xiao, M. N. Hedhili, Q. Jiang, H. N. Alshareef, B. Xu, F. Pan, Y. Gogotsi, *Angew. Chem., Int. Ed.* **2019**, *58*, 17849.
- [24] Y. Liao, J. Qian, G. Xie, Q. Han, W. Dang, Y. Wang, L. Lv, S. Zhao, L. Luo, W. Zhang, H.-Y. Jiang, J. Tang, *Appl. Catal. B* **2020**, *273*, 119054.

- [25] Y. Li, H. Wang, L. Xie, Y. Liang, G. Hong, H. Dai, *J. Am. Chem. Soc.* **2011**, *133*, 7296.
- [26] a) Y. Hu, T. Xiong, M. S. J. T. Balogun, Y. Huang, D. Adekoya, S. Zhang, Y. Tong, *Mater. Today Phys.* **2020**, *15*, 100267; b) Y. Tian, L. Xu, M. Li, D. Yuan, X. Liu, J. Qian, Y. Dou, J. Qiu, S. Zhang, *Nano-Micro Lett.* **2021**, *13*, 3.
- [27] C. Cui, R. Cheng, H. Zhang, C. Zhang, Y. Ma, C. Shi, B. Fan, H. Wang, X. Wang, *Adv. Funct. Mater.* **2020**, *30*, 2000693.
- [28] a) N. Cheng, S. Stambula, D. Wang, M. N. Banis, J. Liu, A. Riese, B. Xiao, R. Li, T. K. Sham, L. M. Liu, G. A. Botton, X. Sun, *Nat. Commun.* **2016**, *7*, 13638.; b) H. Zhang, P. An, W. Zhou, B. Y. Guan, P. Zhang, J. Dong, X. W. D. Lou, *Sci. Adv.* **2018**, *4*, 6657.